nature physics

Article

https://doi.org/10.1038/s41567-023-01954-3

Phase-locked photon–electron interaction without a laser

In the format provided by the authors and unedited

1. Characterizing the EDPHS radiation

A full characterization of the EDPHS radiation generally requires pulse-characterization techniques. Here, we use a simple interferometric technique that is able to demonstrate the degree of coherence of the radiation. Before we get to the experimental results, we first show the simulation results to clarify the collimation and chirping of the radiation pattern of the EDPHS. A time-dependent finite-difference method, which is fully explained elsewhere, is used[1]. The discretization unit cell is 2 nm, and for the calculation a supercomputer at the Kiel University Computing Center is used. 60000 temporal iterations were required to cover the time period of 230 fs, thus allowing convergence. The simulation time was 108 hours.

In contrast to the EDPHS structure reported in ref.[2], here the radiation from the EDPHS is not focused, but it is collimated, as obvious from the angle-resolved pattern shown in Fig. 1 of the main text (Fig. S1a). The collimated EDPHS radiation helps to maintain the same EDPHS beam profile on the sample via changing the distance between the EDPHS and the sample, allowing to systematically investigate the role of decoherence without altering the beam divergence and profile, as shown in section 4 of the supplementary notes. Nevertheless, we have used the same design principle reported before[2], which is based on distributing a two-dimensional array of nanopinholes in a gold thin film (Fig. S1a). The distribution of the holes is determined via an inverse holographic approach[3]. This structure obviously hosts a large number of optical modes that are also energetically distributed in a closed-pack manner, resulting in an inhomogeneous broadening of the near-field spectra; consequently, the far-field radiation from the structure is chirped (Fig. S1b). Windowed Fourier transformation of the time-dependent field demonstrates the down-chirp of the optical radiation (Fig. S1c), where the wavelength of the signal increases with time. As a result, the total spectrum (black solid line) is a broadband excitation with a bandwidth of approximately 200 nm centered at 820 nm, in close agreement with the measured CL spectrum (Fig. 2d). The spatial profile of the EDPHS radiation also captures the collimation of the EDPHS radiation over a broad wavelength range from 700 nm to 1000 nm (Fig. S1d), where at shorter wavelength, the excitation of side lobes is also apparent, causing a diffused radiation pattern at larger polar angular ranges in the angle-resolved CL map.

In order to quantify the coherence length of the EDPHS radiation, we investigate the interaction of the electron beam with two identical EDPHS structures positioned along the path of the electron beam at a distance *L* (Fig. S2a). The far-field radiation from the whole structure is the superposition of the radiations from each individual EDPHS structure, in addition to the scattered field caused by the interaction of the first EDPHS radiation with the second one (Fig. S2b). The acquired momentum-resolved CL map at the filtered wavelength of 800 nm (corresponding to the carrier wavelength of the EDPHS radiation) shows a prominent interference pattern versus the distance between the EDPHS structures, in full agreement with the simulation results (Fig. S2c and d). The agreement between the experimental and simulated results is encoded more prominently in the line profile captured by integrating the CL intensity over the whole momentum axis (Fig. S2e). The distance between the maxima of the interference pattern does not depend on the acquired transverse momentum, showing that the main contribution is caused by the interference between the optical beams that propagate along the same direction, i.e., the collimated beam paths. This effect is in contrast to the case where the WSe_2 flake is used as the sample. For the latter case, as will be discussed later, the interference between waves with dipolar wave fronts such as transition radiations and the scattering of the exciton polaritons from the edges, with directional waves,

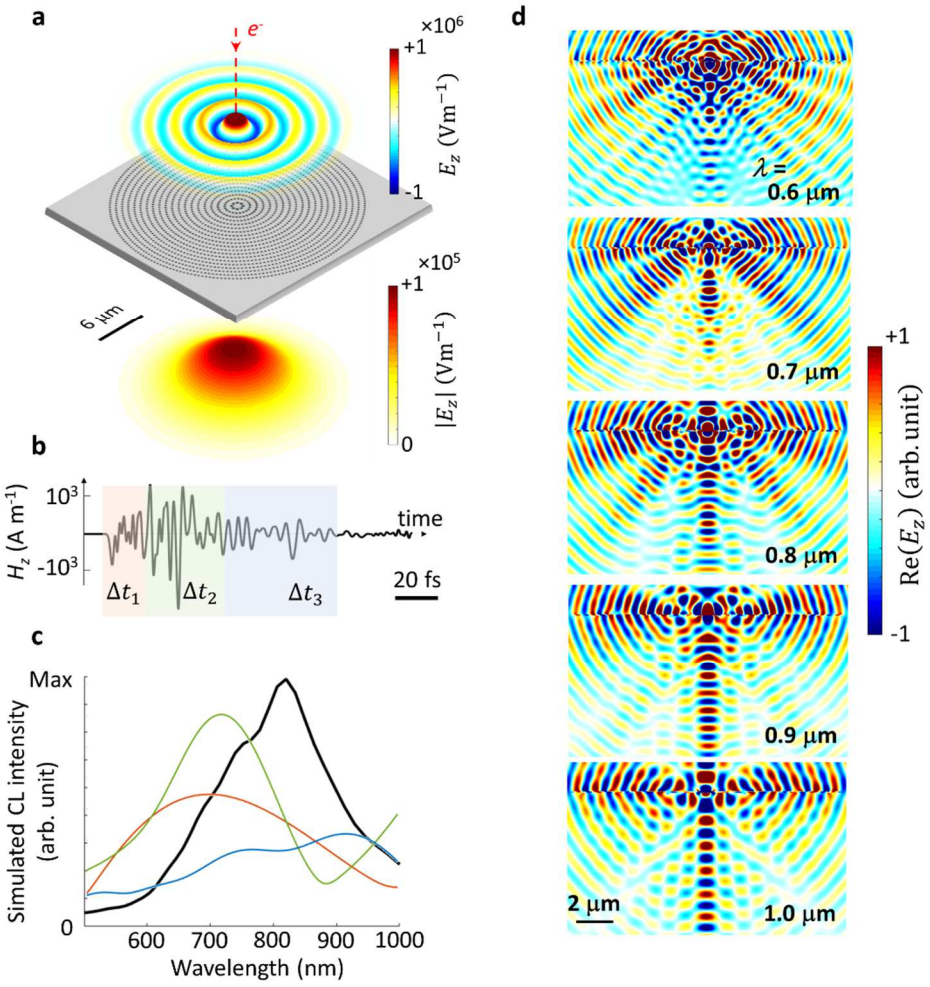

Fig. S1. Numerical simulations showing the collimation and chirping of the EDPHS radiation. (a) EDPHS design based on transforming a radially propagating surface plasmon polariton induced by the electron beam, into a collimated Gaussian beam, via its interaction with a distribution of nanopinholes. (b) Simulated temporal profile of the radiation at the far-field zone, demonstrating a chirp excitation, with its full spectrum (black solid lines) and spectra acquired from the colored window regions shown in (c). (d) Spatial profile of the amplitude of the *z*-component of the electric field at depicted wavelengths and at a given time, where the collimated radiation is obvious.

cause an interference pattern that is significantly $k_{||}$– dependent. The maximum intensity of the interference pattern is only observed after the distance of $22\,\mu\text{m}$ (delay of $\tau = 148\,\text{fs}$) between the EDPHS structures, which corresponds to the required time for the induced polarization in the EDPHS to substantially contribute to the radiation continuum and moreover overlap with the electron induced radiation from the second EDPHS. Since electrons are propagating at the speed of 0.328 *c*, the retardation time for the EDPHS radiation is obtained as $\delta\tau = 22\,\mu\text{m}\left(v^{-1} - c^{-1}\right) = 150\,\text{fs}$. This time onset of the observation of the interference phenomenon directly matches with the experiment that involves the

WSe_2 flake as the second interaction point, and is linked to the retarded time required for the EDPHS structure to contribute to the radiation continuum.

The numerically calculated interference fringes have a higher degree of coherence compared to the experimental results, which is due to the fact that in the simulations we have used a truncated EDPHS structure with a circular boundary. This allows for more light to be transmitted from the first EDPHS to

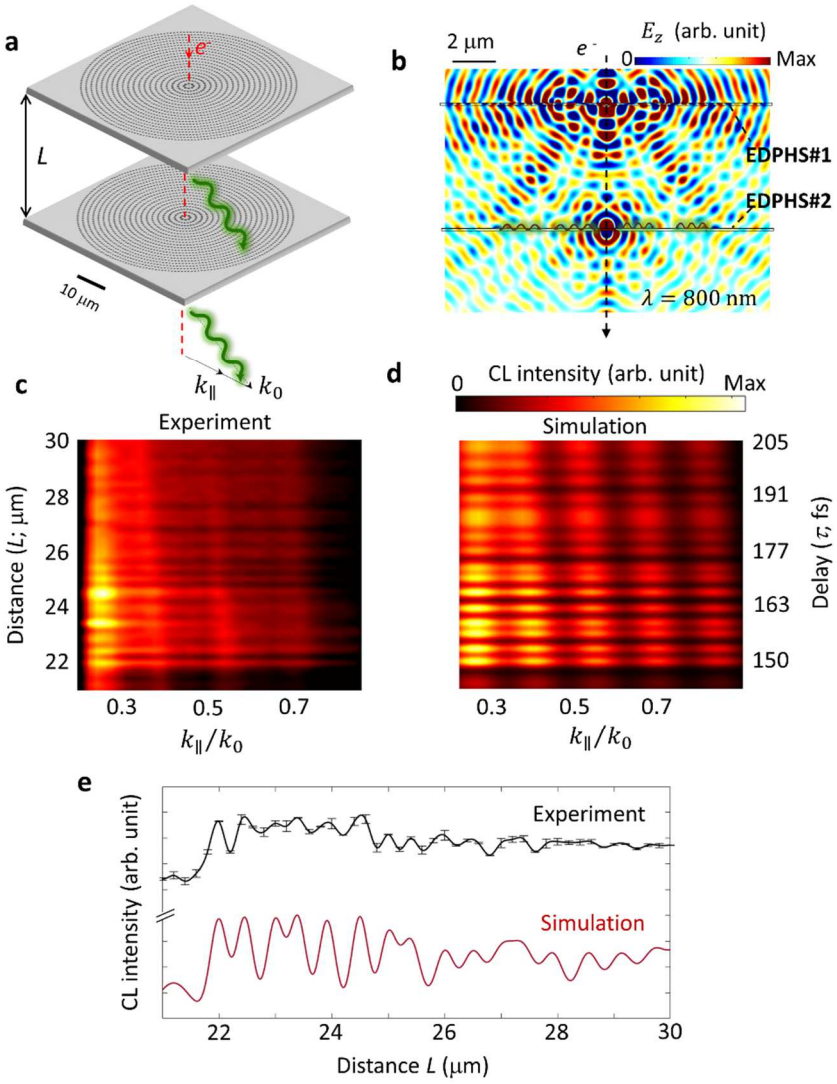

Fig. S2. Characterizing the coherence length of the EDPHS radiation. (a) Two similar EDPHS structures are positioned at distance *L* with respect to each other along the trajectory of the electron beam, where the electron beam interacts with both structures at a delay L/v_{el}. Depending on the delay, the EDPHS radiations interfere constructively or destructively in the far-field. (b) The spatial profile of the *z*-component of the electric field for the double-EDPHS structure, at the wavelength of 800 nm. (c) Measured and (d) simulated CL intensity versus the transverse momentum and the distance *L*. (e) Line profiles of the measured and simulated integrated CL intensities versus the distance.

the detector, in contrast with the experiment, where the radiation of the first EDPHS is partially blocked by the second EDPHS due to its closed configuration (see Fig. S2a).

2. Phase-locked photon-electron spectroscopy setup

Our phase-locked photon-electron spectroscopy setup is based on the integration of a nanopositioner system with a cathodoluminescence detection unit. We have designed a vacuum-compatible compact piezo stage in collaboration with the SmarAct Company[1], with three axial degrees of freedom, 1 nm accuracy in the step size, and a dynamic range of 12 mm (Fig. S3a and b). The electron-driven photon source (EDPHS) is held by a solid arm by the nanopositioner and its lateral and vertical positions with respect to the sample are precisely controlled. The position of the sample is controlled by the SEM sample stage (Fig. S3a and b). Our system is equipped with two parabolic mirrors that collect the photons emitted by the combined SEM/EDPHS system (Fig. 3c), though only either the top or the bottom mirror is used for each experiment. The mirror positioned on top of the stage has a larger photon collection efficiency. The mirror positioned below the sample – used in the present measurements – has a larger hole in the middle, to avoid damage upon electron-beam irradiation.

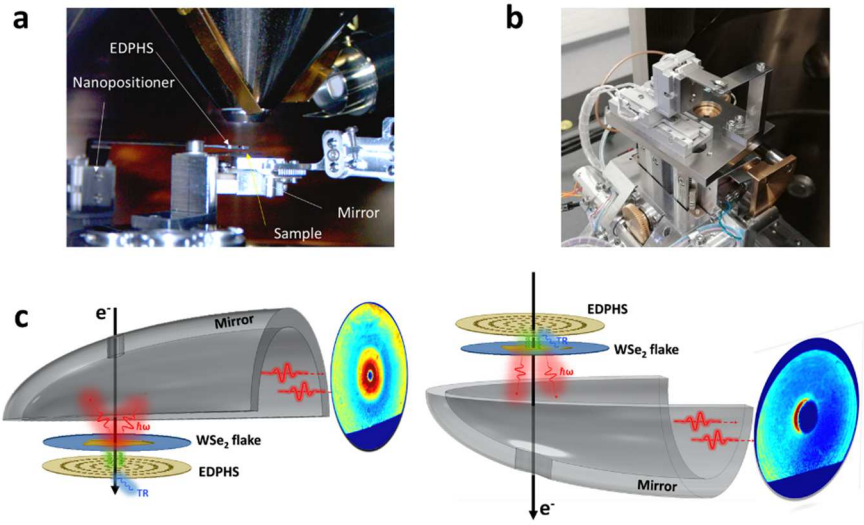

Fig. S3. Correlative photon-electron spectroscopy setup. (a) Schematic of the setup positioned in the chamber of the electron microscope, including a nanopositioner piezo stage for aligning the EDPHS position with respect to the electron beam and the sample. (b) Nanopositioner positioned on the sample stage of the electron microscope. (c) Collector mirrors located above (left) and below (right) the sample, and the angle-resolved CL pattern of the EDPHS structure as captured by both mirrors.

[1] https://www.smaract.com/index-en

3. Exciton polaritons in WSe_2 thin films

High-quality crystals of 2*H*-WSe_2 were grown by the standard chemical vapor transport method. Thin nanosheets were prepared by applying liquid phase exfoliation (LPE) from the bulk WSe_2 in isopropanol (Merck, ≥ 99.8%). Exfoliation was performed with an ultrasonicator (320 W, Bandelin Sonorex, RK100H) equipped with a timer and heat controller to avoid solvent evaporation. The resulting suspension was drop casted on a holey carbon mesh grid for further characterization.

Exciton-photon interactions are categorized into weak- and strong-coupling regimes, where the former happens for the scattering of light from excitons in free space, and the latter could be obtained when the excitons, normally considered as two-level systems, are positioned inside a Fabry-Perot cavity. Due to the increased interaction time, which can be estimated by the finesse of the cavity, the effective absorption cross section of the excitons is increased, and the interaction leads to new hybridized exciton-cavity states. To reach the strong-coupling regime with a number of N_a emitters inside a cavity, the criterion to be met is $N_a C = N_a g^2 / 2\kappa\gamma \gg 1$, where $g = \sqrt{\mu^2\omega / 2\varepsilon_0 \hbar V}$ is the exciton-cavity Rabi frequency, $\kappa = \pi c / 2LF$, and $\gamma = \mu^2\omega^3 / 6\pi\varepsilon_0\hbar c^3$ is the spontaneous decay rate of the excitons[4]. The parameter L, the length of the cavity (here, the thickness of the film) drops out, as it appears also in the parameter $V = L \cdot A^2$, the volume of the cavity. F is the finesse of the cavity, which can be calculated by the reflection coefficients at the WSe_2/air interface (Fig. S4a and b). Obviously, due to the large refractive index of WSe_2, the criterion for the total internal reflection is easily met. Nevertheless, the material loss directly affects the performance of the cavity in general and hence the finesse is also affected by the loss inside the cavity (Fig. S4b). Considering 100 emitters within an area of $A = 1\,\mu\text{m} \times 1\,\mu\text{m}$ of the cavity, the criterion

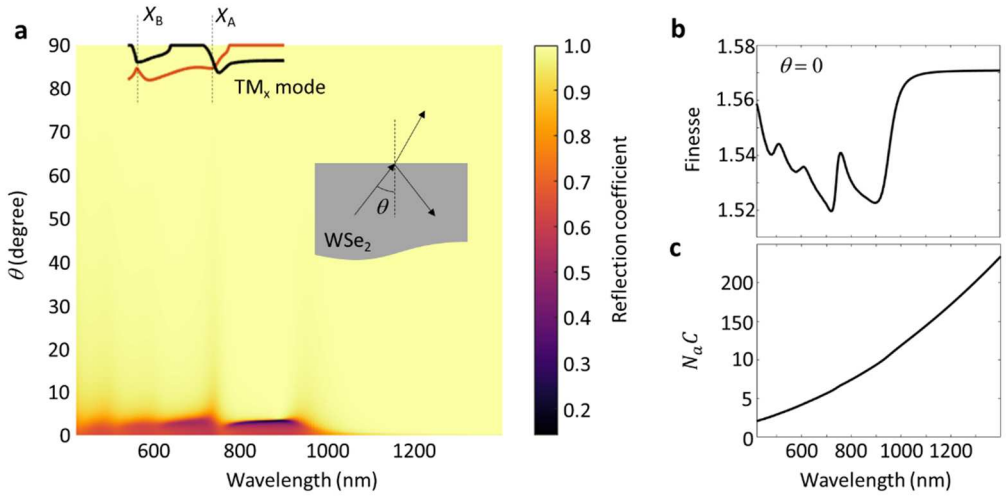

Fig. S4. Strong-coupling criterion for exciton-photon interactions in WSe_2 thin films. (a) Reflection coefficient for an interface between WSe_2 and air. Solid lines show the angle-wavelength dependence associated with the TM$_x$ mode of a WSe_2 thin film with the thickness of *d* = 80 nm. (b) The finesse parameter associated with a symmetric WSe_2 film, holding Fabry-Perot like resonances at $\theta = 0$. (c) Cooperativity parameter for a number of 100 excitonic emitters inside a volume of $d \times (1\ \mu\text{m})^2$ of the optical cavity (thin film).

mentioned above could be met for $\lambda > 600\,\mathrm{nm}$. Moreover, the coupling efficiency increases with increasing the wavelength, providing the reason for the stronger interactions between A excitons and photons, compared to B excitons.

Due to strong exciton-photon interactions in the WSe_2 flakes, lower-polariton (LP) and upper-polariton (UP) branches are formed, and the corresponding propagation mechanisms in thin films can be probed by CL spectroscopy[5] (Fig. S5a, b and c). Particularly comparing the absorption spectrum (Fig. S5d) with the CL spectrum (Fig. S5c), the strong interaction between light and the cavity modes and its signature on the CL spectra become apparent. Moreover, the interaction of the propagating polaritons with the edges of the flakes is obviously tracked by scanning the sample with the electron beam and acquiring the CL spectra at each point. Strong interactions between photons and excitons can be probed in the time domain by observing Rabi oscillations. Spectral signatures of Rabi oscillations include an energy splitting and level repulsion in the reciprocal domain that becomes apparent by the energy splitting observed in the CL spectra (Fig. S5c). The amount of the energy splitting between LP and UP branches determines the exciton-photon coupling strength that varies as a function of the distance from the edge of the flake. The dispersion of the exciton polaritons in such a thin film is analytically calculated (Fig. S5e) and perfectly demonstrates the level repulsion caused by the coupling between the photonic mode of the thin film (black dashed line) and the excitons (solid green lines). The propagating exciton polaritons are partially reflected from the edges of the flake and partially scattered to the far-field (Fig. S5f and g). Particularly, the interferences observed in the far-field angle-resolved map can be understood by the interference between the transition radiation and the scattering of the exciton polaritons from the edges of the flakes.

Transition radiation (TR) is the radiation caused by the time-varying dipole, formed by the interaction between the swift electron and its image inside the material, when the electron approaches the surface of the material. The annihilation of this dipole when the electron reaches the surface of the material creates ultrafast radiation that covers the spectral range from a few meV to several eVs[6], having a dipolar-like radiation pattern[7]. Transition radiation has been recently used to retrieve the spatial phases attributed to plasmonic excitations[8]. Within the WSe_2 flakes, the excited transition radiation can interfere with the scattered exciton polaritons from the edges of the flakes. Since the electron-induced exciton polaritons sustain a radial wave front, a simple model can be constructed to retrieve the far-field interference pattern, by assuming that the superposition of the scattered waves from the edges of the flake and the transition radiation can be formulated as

$$\psi\left(\vec{r},\theta\right) = \frac{e^{-ik_0 r}}{4\pi r}\sin\theta\left(1+\left|T_2\right|e^{ik_0\sin\theta l - i\left(\beta - i\alpha\right)l + i\varphi_{T_2}}\right). \tag{S1}$$

Therefore, the maxima of the far-field interference pattern are recast as

$$\beta\left(\omega\right)l = k_0\sin\theta l + 2n\pi + \varphi_{T_2} \tag{S2}$$

where $\beta\left(\omega\right) - i\alpha\left(\omega\right)$ is the frequency-dependent complex-valued propagation constant of the exciton polaritons (Fig. S2e). Its real part, i.e., the phase constant $\beta\left(\omega\right)$, is the difference in phase per meter of the propagation of the polaritons in the thin film. $\alpha\left(\omega\right)$, i.e., the attenuation constant, models the

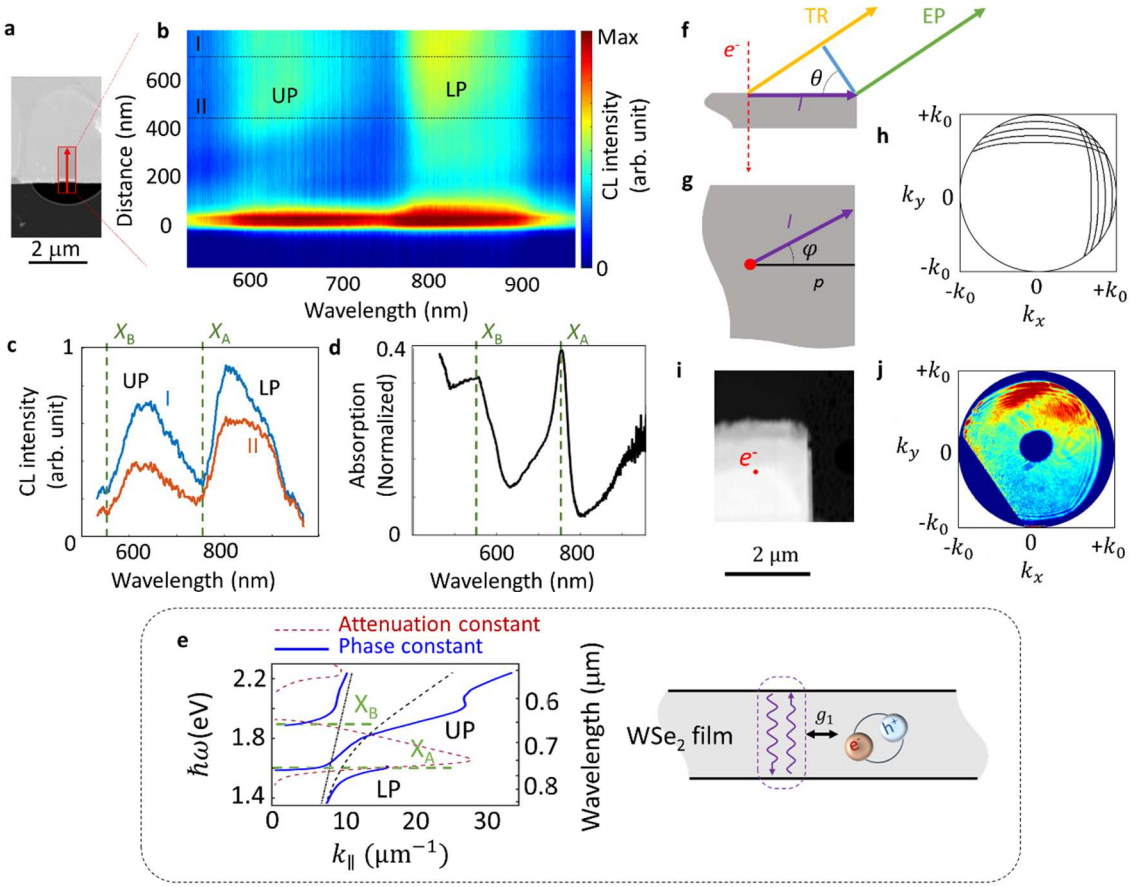

Fig. S5. Exciton polaritons in the WSe_2 flake. (a) SEM image of the sample, composed of a WSe_2 flake positioned on top of a holey carbon substrate. (b) CL spectra at different scanning positions of the electron beam. The sample is scanned along the scanning direction marked by the red arrow in (a) and integrated along the vertical direction. The formation of the LP and UP branches in the spectral regions marked by UP and LP, respectively, is apparent. (c) CL spectra at depicted electron impact positions marked by I and II in (b). (d) Absorption coefficient of the flake measured by using an all-optical dark-field microscopy/spectroscopy setup. (e) Propagation constant ($\beta - i\alpha$) of the exciton polaritons versus the photon energy ($\hbar\omega$), β (the phase constant) and α (the attenuation constant) are shown by thick solid blue and dashed red curves, respectively. The optical line ($k_0 = \omega/c$) is indicated by a thin dashed-dotted black curve, and the dispersion of the photonic modes, due to the background permittivity $\varepsilon_{r,\infty} = 15$, is represented by a thin black dashed curve. X_A and X_B excitonic energies are marked by dashed green lines. (f) Radiation mechanisms are attributed to the transition radiation (TR; orange arrow), the excitation of exciton polaritons (purple arrow) and their scattering at the edge of the flake (green arrow). Shown is the lateral view. (g) Top view with the electron impact position shown by the red dot. The exciton polaritons propagating at an elevated angle φ with respect to the normal to edge take the path length $l = p/\cos\varphi$ to reach the edge. (h) The position of the maxima of the interference maps modeled by assuming constructive interference between TR and the exciton polaritons at the far-field. The electron impact parameter is chosen to be $p = 1.6\ \mu m$ from both edges. (i) SEM image of the WSe_2 flake used to evaluate the TR/exciton-polariton interference hypothesis. (j) Angle-resolved CL pattern acquired at $\lambda = 800\ \text{nm} \pm 10\ \text{nm}$.

attenuation of the polaritons per meter of their propagation, due to the materials dissipation or radiation loss. $|T_2|e^{i\varphi_{T_2}}$ is the complex-valued transmission coefficient of the *z*–component of the electric field (this term will be discussed in Supplementary Note S4), $l = p/\cos\varphi$ is the propagation length of the exciton polariton (Fig. S5f and g), with p being the electron impact parameter with respect to the edge, φ the azimuthal angle, and θ the polar angle. Considering two edges, the angular profile in the far-field zone attributed to the maxima of the constructive interference events are obtained and indicated by the contours shown in Fig. S5h, where $p = 1200\,\mathrm{nm}$ has been considered. The position of these contours matches well with the experimentally observed interference patterns in the angle-resolved CL maps, where only up to *n* = 3 interference orders are observed (Fig. S5i and j).

4. Mutual coherence and simulated interference map

Commonly, the visibility of the interference fringes determines the degree of coherence in all experiments involving a superposition of coherent waves. More precisely, the mechanism of decoherence can be tracked by observing how the visibility of the interference fringes is altered by systematically changing a control parameter, i.e., the distance between the individual components of a superposition. Thus, in our experiment, tracking the visibility of the interference fringes by altering the distance between the EDPHS and the sample allows us to determine the mutual coherence between the EDPHS and the sample radiation, and more prominently, observing the decoherence phenomena due to the interaction of the sample (and the EDPHS) excitations with the environment.

The environment in our experimental geometry involves all processes that occur outside the closed system of exciton polariton excitations with the EDPHS and the electron beam. This includes, for example, phonon excitations in the WSe_2 flake and the substrate, the optical excitations in the substrate such as scattering from a distribution of holes with various geometries, and the geometry of the TEM grid as well. The latter includes an array of squares of approximately $20\ \mu\mathrm{m} \times 20\ \mu\mathrm{m}$ each.Excited exciton polaritons that are scattered from the edge of the flake, interact with all the other scattering objects that are located in our setup. Additionally, radiative decay of excitons also contributes to loss of coherence.

As mentioned in the main text, the angle-resolved radiation pattern can be divided into three domains (Fig. S6a and b): (i) in the region between $L = 22\ \mu\mathrm{m}$ and $40\ \mu\mathrm{m}$, the interference pattern is sharply altered, caused by the influence of the EDPHS radiation; (ii) in the range between $L = 40\ \mu\mathrm{m}$ and $52\ \mu\mathrm{m}$, the visibility of the interference fringes is completely diminished, (iii) followed by the backscattered waves caused by the TEM sample grid, the substrate, and possibly other flakes positioned on the holy carbon substrate, obvious in the range from $L = 52\ \mu\mathrm{m}$ and $120\ \mu\mathrm{m}$.

The visibility of the interference fringes in a spectral interferometry technique versus the delay between the optical pulses is not related to the overlap of the optical pulses in the temporal domain. Indeed, for the case of $\tau = 0$, i.e., the maximum temporal overlap, no interference effect in the spectral domain is observed. Thus, the reduced visibility of the interference pattern by altering the delay between the optical pulses can be related only to decoherence which arises due to interaction with the environmental bath.[9,10].

The observed far-field interference patterns, could be modeled as a superposition of the scattered waves from the flake, initiated by both the EDPHS and the flake (Fig. S7a). The contribution of the electron beam

to the scattered waves are modeled by both transition radiation and the exciton polaritons scattered from the edge. Generalizing eq. (S1), for the case of a thinner flake, where the excited exciton polaritons could get scattered from both edges of the thin ribbon shown in Fig. 2a, we derive the electron induced CL as

$$\psi^{\mathrm{el}}\left(\vec{r},\theta\right)=\frac{e^{-ik_0 r}}{4\pi r}\sin\theta\left\{1+e^{ik_0\sin\theta\, l_1-i(\beta-i\alpha)l_1}\sum_{n=0}^{+\infty}\left|T_2\right|\left|R_2\right|^{2n}e^{-i(\beta-i\alpha)2nl_2}e^{i\varphi_{T_2}+i2n\varphi_{R_2}}\right.$$
$$\left.+e^{ik_0\sin\theta(l_2-l_1)-i(\beta-i\alpha)(l_2-l_1)}\sum_{n=1}^{+\infty}\left|T_2\right|\left|R_2\right|^{2n}e^{-i\beta 2nl_2}e^{i\varphi_{T_2}+i2n\varphi_{R_2}}\right\}, \qquad \text{(S3)}$$

where, the first term on the RHS, is due to the transition radiation. Each term in the first series is associated with the exciton polaritons with the phase constant β that represent the scattering from the right edge of the flake after travelling *n* times through the flake and reflecting back from the left edge.

The scattering from the edge of the flake is modeled by its transmission and reflection coefficients, $\left|T_2\right|e^{i\varphi_{T_2}}$ and $\left|R_2\right|e^{i\varphi_{R_2}}$ (Fig. S7b and c), respectively. The third term is due to the scattering of the exciton polaritons from the left side of the flake. The EDPHS scattered field can be modeled as

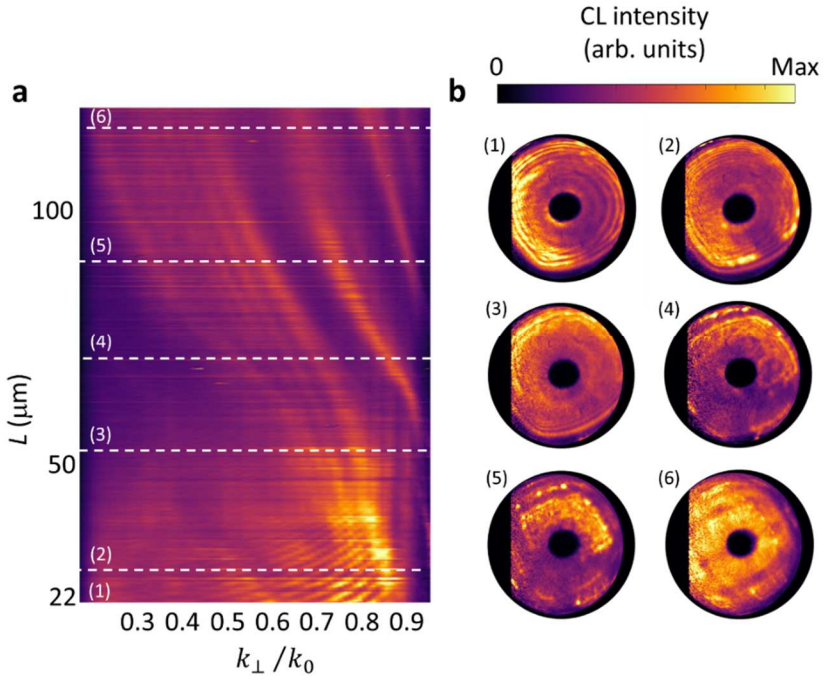

Fig. S6. Mutual coherence and decoherence effects in EDPHS-sample interactions. (a) Angle-resolved CL patterns at the wavelength of $\lambda = 800$ nm, versus the distance, integrated over the azimuthal angle range of 95° to 100°, and (b) at depicted distances *L* between the EDPHS and the sample, demonstrating the modulation of the interferences patterns versus *L*.

$$\psi^{\mathrm{EDPHS}}\left(\vec{r},\theta\right)=\frac{e^{-ikr}}{4\pi r}\sin\theta\left\{\left|T_1\right|e^{i\varphi_{T_1}}+e^{ik_0\sin\theta l_1}\sum_{n=1}^{+\infty}\left|T_2\right|\left|R_2\right|^{2n-1}e^{-i(\beta-i\alpha)2nl_2}e^{i\varphi_{T_2}+i(2n-1)\varphi_{R_2}}\right.$$
$$\left.+e^{ik_0\sin\theta(l_2-l_1)-i(\beta-i\alpha)(l_2-l_1)}\sum_{n=0}^{+\infty}\left|T_2\right|\left|R_2\right|^{2n}e^{-i(\beta-i\alpha)2nl_2}e^{i\varphi_{T_2}+i2n\varphi_{R_2}}\right\}, \tag{S4}$$

where the first term is due to the direct transmission through the flake. Its transmission and reflection coefficient are hence only frequency-dependent, due to the materials dispersion, and not dependent on the scattering angle θ. Moreover, the T_2 and R_2 coefficients are only frequency-dependent, since the incident angle θ_1 is related to the phase constant as $\theta_1=\beta(\omega)\Big/\left(\sqrt{\varepsilon_r(\omega)}k_0\right)$, where $\varepsilon_r(\omega)$ is the material permittivity. The total radiation is thus calculated as $\left|\psi\right|^2=\left|\psi^{\mathrm{el}}+e^{i\omega\tau}\psi^{\mathrm{EDPHS}}\right|^2$, with the delay given by $\tau=L\left(v^{-1}-c^{-1}\right)$. EDPHS radiation can also excite exciton polaritons, when the radiation is scattered from the edge of the flake, which is justified due to the transverse broadening of the EDPHS radiation (yellow circle in Fig. 2a). Thus, in first order (*n* = 0), only scattering from the right side of the flake is possible for the electron beam contribution, and the scattering from the left side is included in the EDPHS contribution. Figure S8 shows the comparison between two cases: (i) only scattering from the right side of the grid is included and terms up to *n* = 1 are considered, and (ii) scattering from the right side of the grid is also included, but still only terms up to the *n* = 1 are included. To calculate the transmission coefficients through the edge, the edges are modeled as an infinite interface. However, in reality the radiation will be in the form of a dipole oriented parallel to the edge of the flake, for flakes thinner than 100 nm, when the higher order multipolar excitations could be neglected. Thus, the dipole radiation pattern $\sin\theta$ is also retained for the scattered waves from the edge. The comparison between the cases, shows that indeed the major contribution is due to the scattering from the right side of the flake, though the scattering from the left side could cause lower frequency modulations along the $k_{\parallel}$ axis, in better agreement with the simulation and experimental results.

The angle-resolved maps acquired at fine steps of 100 nm within the range of $L=0\ \mu\mathrm{m}$ to $150\ \mu\mathrm{m}$, required 36 hours of continuous measurements, where sample drift and beam instabilities might undermine a full agreement with the theoretical results, though apparently are minor issues due to our drift correction mechanism.

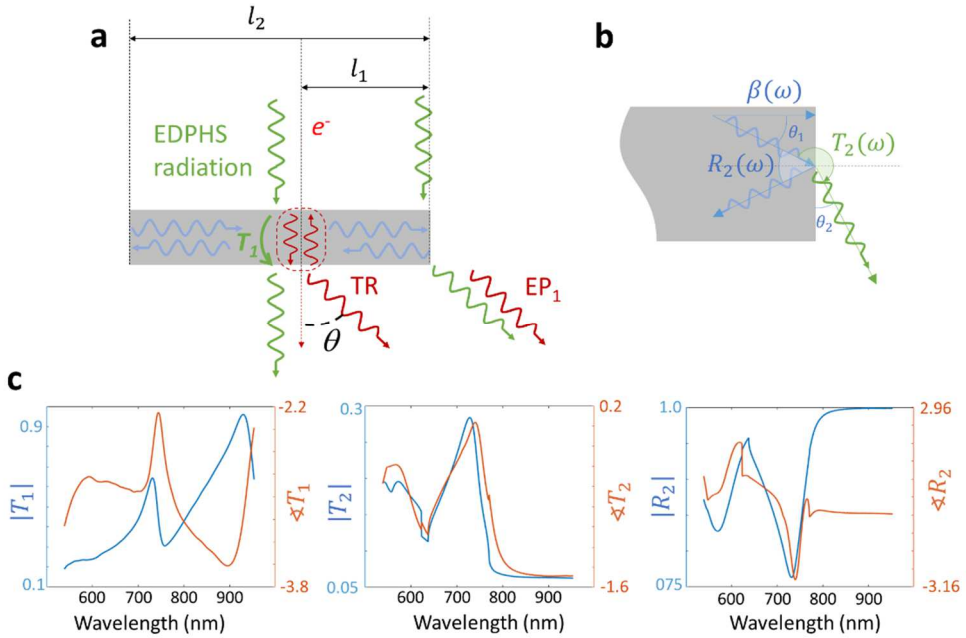

Fig. S7. Optical pathways contributing to the overall CL pattern. (a) Schematic of possible scattered beams, caused by the EDPHS radiation (green wavy arrows) and the electron beam (red wavy arrows). The blue wavy arrows show the excited guided mode of the thin film, to which both the electron beam and the EDPHS contribute. (b) Schematic of transmitted and reflected optical rays at the edge of the flake. (c) Analytically calculated amplitude and phase of the transmission and reflection coefficients T_1, T_2 and R_2.

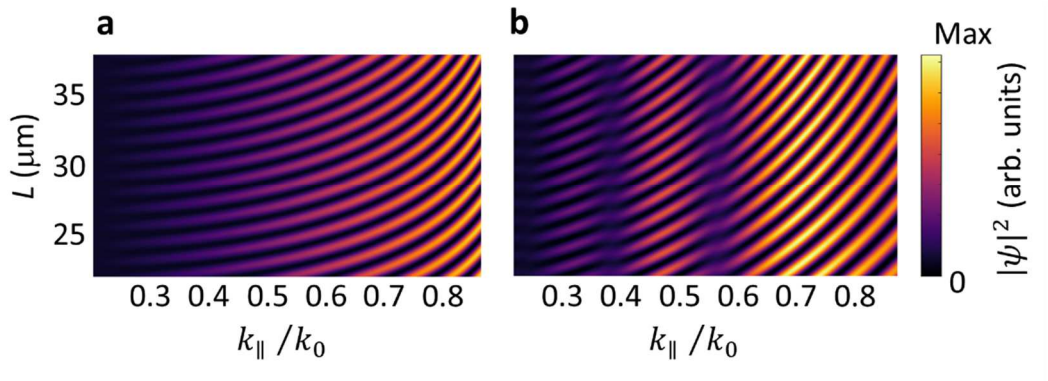

Fig. S8. Analytically calculated interference fringes, (a) including only radiation from the right side and (b) radiation from both the right and left sides of the flake.

5. Inventory

High resolutions images and source codes are available for some of the individual main text figures in the following repository addresses:

Fig. 1d: 10.6084/m9.figshare.21828867

Fig. 1f: 10.6084/m9.figshare.21828888

Fig. 2e: 10.6084/m9.figshare.21828879

Fig. 4b: 10.6084/m9.figshare.21828876

Fig. 4c: 10.6084/m9.figshare.21828882

Fig. 4d: 10.6084/m9.figshare.21828885

Fig. 4e: 10.6084/m9.figshare.21828870

Fig. 4f: 10.6084/m9.figshare.21828873

References:

1 Talebi, N., Sigle, W., Vogelgesang, R. & van Aken, P. Numerical simulations of interference effects in photon-assisted electron energy-loss spectroscopy. *New Journal of Physics* **15**, 053013, doi:10.1088/1367-2630/15/5/053013 (2013).

2 Talebi, N. *et al.* Merging transformation optics with electron-driven photon sources. *Nature Communications* **10**, 599, doi:10.1038/s41467-019-08488-4 (2019).

3 Li, G., Clarke, B. P., So, J.-K., MacDonald, K. F. & Zheludev, N. I. Holographic free-electron light source. *Nature Communications* **7**, 13705, doi:10.1038/ncomms13705 (2016).

4 Reiserer, A. & Rempe, G. Cavity-based quantum networks with single atoms and optical photons. *Reviews of Modern Physics* **87**, 1379-1418, doi:10.1103/RevModPhys.87.1379 (2015).

5 Taleb, M., Davoodi, F., Diekmann, F. K., Rossnagel, K. & Talebi, N. Charting the Exciton–Polariton Landscape of WSe2 Thin Flakes by Cathodoluminescence Spectroscopy. *Advanced Photonics Research* **3**, 2100124, doi:https://doi.org/10.1002/adpr.202100124 (2022).

6 Kuttge, M. *et al.* Local density of states, spectrum, and far-field interference of surface plasmon polaritons probed by cathodoluminescence. *Physical Review B* **79**, 113405, doi:10.1103/PhysRevB.79.113405 (2009).

7 García de Abajo, F. J. Optical excitations in electron microscopy. *Reviews of Modern Physics* **82**, 209-275, doi:10.1103/RevModPhys.82.209 (2010).

8 Schilder, N. J., Agrawal, H., Garnett, E. C. & Polman, A. Phase-Resolved Surface Plasmon Scattering Probed by Cathodoluminescence Holography. *ACS Photonics* **7**, 1476-1482, doi:10.1021/acsphotonics.0c00209 (2020).

9 Kerker, N., Röpke, R., Steinert, L. M., Pooch, A. & Stibor, A. Quantum decoherence by Coulomb interaction. *New Journal of Physics* **22**, 063039, doi:10.1088/1367-2630/ab8efc (2020).

10 Sonnentag, P. & Hasselbach, F. Measurement of Decoherence of Electron Waves and Visualization of the Quantum-Classical Transition. *Physical Review Letters* **98**, 200402, doi:10.1103/PhysRevLett.98.200402 (2007).